Version of Record: https://www.sciencedirect.com/science/article/pii/S2352431622000633
Manuscript_72e5b35285ff3d4f32bfce8a664eb10f

Hexagonal Ring Origami – Snap-folding with Large Packing Ratio

Shuai Wu[1]†, Jize Dai[2]†, Sophie Leanza[2]†, Ruike Renee Zhao[1]*

[1] Department of Mechanical Engineering, Stanford University, Stanford, CA, 94305.
[2] Department of Mechanical and Aerospace Engineering, The Ohio State University, Columbus, OH, 43210.

* Corresponding author. Email: rrzhao@stanford.edu.
† These authors contributed equally to this work.

Abstract

Hexagonal and hexagon-based structures are widely seen in nature and inspire various engineering designs by demonstrating capabilities of tessellating complex two-dimensional (2D) and three-dimensional (3D) assemblies. While enabling functionality at the deployed state, folding hexagonal structures to a greatly reduced area or volume allows for space-saving for transportation. However, the study on an effective folding strategy is limited. In this work, we report a snap-folding strategy for hexagonal rings, which results in a folded state with only 11% of the initial area. Through finite element analysis and experimental validation, the influence of geometric parameters, loading methods, and loading locations on the hexagonal rings' foldability and stability is investigated systematically. Triggered by buckling instability under bending or twisting, hexagonal rings demonstrate precise and self-guided folding with high flexibility and a high tolerance to loading fluctuations. It is anticipated that the hexagonal ring origami could provide a new strategy for designing functional large foldable structures with self-guided deformation and an excellent packing ratio.

Keywords: hexagonal ring origami, tessellation, foldable structures, bistability, buckling instabilities

1 Introduction

Hexagonal and hexagon-based geometries and structures have been widely seen in nature. For example, honeycomb consists of hexagonal prismatic building blocks [1]; clusters of insect eggs show a compact hexagonal arrangement [2]; compound eyes of insects are tessellated by hexagonal microlens [3]. Nature favors hexagon shape mainly due to its capability of tessellating two-dimensional (2D) or three-dimensional (3D) surfaces without any gap or overlap. In addition, the hexagon shape has the largest area-to-perimeter ratio among basic geometries that can provide gapless tessellations. Thus, the hexagon provides a material-saving strategy and efficient use of space when constructing 2D or 3D architectures. These structural advantages of hexagon shape also inspire engineering designs such as the James Webb space telescope [4], biomimetic artificial compound eyes [5, 6], and honeycomb-like metamaterials [7, 8].

In recent years, foldable structures have drawn significant research attention for many engineering applications such as active metamaterials [9-11], reconfigurable electronics [12, 13], soft robotics [14-16], biomedical devices [17], and space structures [18, 19] for the highly desired merits such as tunable properties and space-saving for transportation purposes. Many folding and reconfiguration mechanisms have been developed for foldable structures. Most origami and kirigami structures rely on a continuous input of external mechanical load for structural shape transformation [20, 21], which is not applicable to specific scenarios when precise and autonomous folding is needed. Stimuli-responsive materials are also explored as a strategy to drive structures by an external field [22-27], allowing remotely controlled folding or deploying. Another strategy features folding of multi-stable structures, which depends on buckling of designed geometries for self-guided deformations towards a state with locally minimized energy [28-32].

Recently, ring origami emerges as a robust folding strategy for closed-loop regular-shaped rods with large packing ratios for different shapes such as circular, elliptical, rectangular, and triangular rings [33]. Ring origami uses snap-folding mechanism that is triggered by the buckling instability of rods under either bending or twisting load. It is demonstrated that the snap-through instability leads to a self-guided folding behavior, which results in a stable three-fold configuration for rings with rationally designed geometric parameters. The packing ratio can be very large with the enveloped folded area only 11% of the initial area. Although hexagon allows for tessellating functional 2D and 3D assemblies, there is limited study exploring effective strategy for folding/deploying of hexagonal and hexagon-based structures [34-40]. In this work, we report the hexagonal ring origami by adopting the snap-folding concept, which enables foldable 2D and 3D assemblies for a large packing ratio, as shown in **Fig. 1**. Here, the complex structure can first be stacked into a configuration of overlapped hexagonal rings. Then, the overlapped hexagonal rings can be folded into a stable peach core-shaped configuration, leading to a folded area that is only 11% of the initial hexagon area. Note that a polygon ring with an edge number of $3n$ ($n \geq 2$ and is an integer) allows for folding into three overlapping rings that is about 11% of the initial area. Folding other polygon rings leads to a lower packing capability due to failure of folding into three overlapping rings. Video S1 shows the self-guided snap-folding and deploying of a foldable hexagonal ring via various loading methods. Understanding the mechanical behavior of the hexagonal ring with different geometric parameters under different loading methods is crucial for the design of their functional 2D and 3D assemblies.

In this work, we use finite element analysis (FEA) to systematically investigate how geometric parameters, loading locations, and loading methods affect the foldability and stability of hexagonal rings. We start from bending-induced snap-folding with varied aspect ratios of

rectangular cross-sections, ring sizes, and rounded corner radii of hexagonal rings. The folding is validated by experimentally bending a 3D-printed ring (see Appendix for details on ring fabrication). Next, we study the influence of bending locations on the snap-folding behavior of hexagonal rings, including corner and middle of edge that pass the hexagon centerline, as well as positions offset from these respective locations. Finally, an alternative folding method, twisting-induced snap-folding of hexagonal rings, is studied via FEA and experimentally verified. The hexagonal rings demonstrate precise and self-guided folding with high flexibility of folding methods and a high tolerance of loading fluctuation. We anticipate the hexagonal ring origami folding mechanism could provide a new strategy for foldable/deployable 2D and 3D structures with a high packing ratio, potentially for future aerospace, biomedical, and robotic applications.

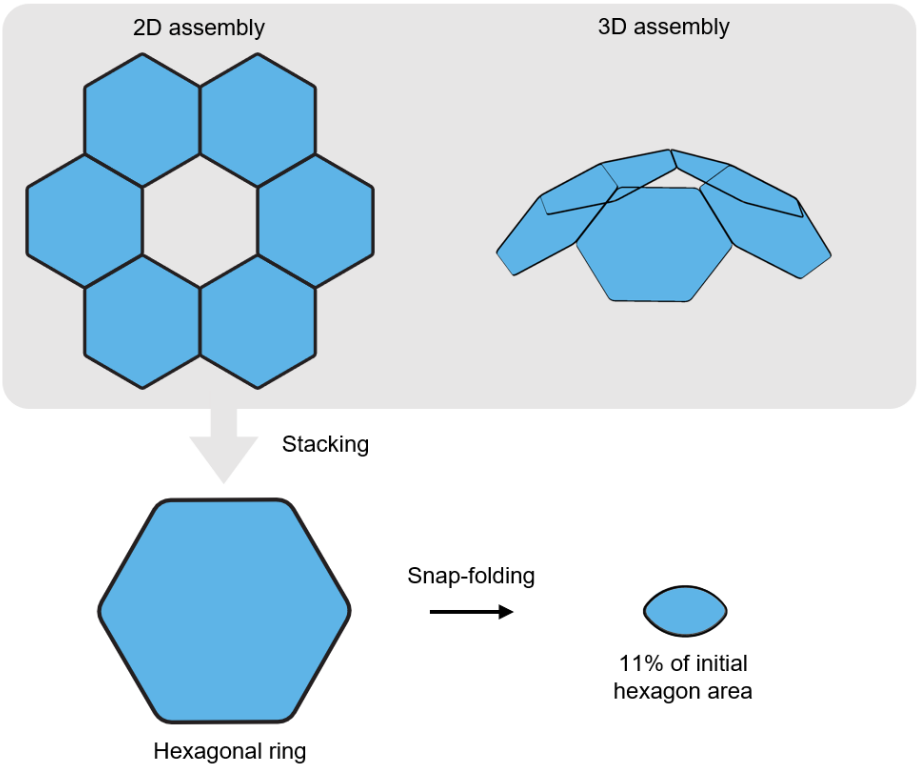

Fig. 1. Concept of hexagonal ring origami for two-dimensional and three-dimensional assemblies with a high packaging ratio. The six-ring 2D assembly and five-ring 3D assembly can be both stacked into a configuration of overlapped hexagonal rings. The overlapped hexagonal rings can then be folded into a peach core-shaped configuration, leading to only 11% of the initial hexagon

area. The packing of the six-ring 2D assembly and five-ring 3D assembly are calculated as 1.8% initial area and 0.004% initial volume, respectively.

2 Bending-induced Snap-Folding of Hexagonal Rings

2.1 Influence of hexagonal ring geometry on bending-induced folding

We start with bending-induced snap-folding of hexagonal rings, investigating how geometric parameters affect the foldability and stability of hexagonal rings (**Fig. 2**). As shown in **Fig. 2a**, the hexagonal ring has an edge length of a, a corner radius of r, and a rectangular cross-section with height of h and thickness of t. To induce folding in FEA, a pair of rotations about the y-axis (dashed blue line) is applied on two corners of the hexagonal ring in opposite directions. Note that the bending angle θ from 0 to π is prescribed at two corners that pass the centerline of the hexagon. Corresponding reaction moment M is exported from FEA, and the two loading positions are free to translate along the x-axis direction. Bending at different locations is studied in the next section. We first vary cross-section aspect ratios (h/t = 1, 1.5, 2, 5, and 8) while fixing the corner radius (r/a = 0.3) and the overall ring size (a/t = 200). The normalized moment (Ma/EJ) is plotted with respect to the bending angle (θ), and corresponding deformed configurations at $\theta = \pi$ are shown in **Fig. 2b**, where E is the Young's modulus and J is the torsion constant. J is calculated as:

$$J = \frac{ht^3}{3}\left(1 - \frac{192}{\pi^5}\frac{t}{h}\sum_{n=1,3,5}^{\infty}\frac{1}{n^5}\tanh\frac{n\pi h}{2t}\right).$$

Note that the normalized moment-bending angle curves apply to rings with different materials. Ring material with a larger stiffness would lead to a higher moment during the snap-folding process. See Fig. S1 for detailed bending-induced folding processes with varied cross-section aspect ratios. In general, with a higher h/t value, the ring shows higher foldability and stability at

the folded state. When h/t = 1 (blue curve), the monotonically increasing normalized moment indicates an un-foldable behavior of the hexagonal ring. As shown in **Fig. 2b**, for a foldable ring (h/t = 1.5, 2, 5, and 8), the normalized moment first increases with the bending angle, and then drops rapidly after the snapping point, which corresponds to the snap-folding into the peach core-shaped configuration. For hexagonal rings with h/t = 1.5 and 2 (orange and green curves), the normalized moment rapidly decreases toward zero without passing zero after the snapping point, implying a foldable but unstable behavior. The folded ring has a peach core-shaped configuration that is 11% of the initial area. With higher cross-section aspect ratios of h/t = 5 and 8 (black and pink curves), hexagonal rings are stable after snap-folding as the moment returns to zero, showing the same folded configuration with 11% of the initial area. It is also seen that a larger h/t value leads to an earlier snapping point and a smaller normalized moment at the snapping point.

We further how varying corner radius influences the rings' foldability and stability. Here, we use one of the foldable rings (h/t = 5, r/a = 0.3, a/t = 200) with varying corner radius r/a =0.05, 0.1, 0.2, 0.3, and 0.4. We observe that varying the corner radius does not change the overall landscape of the normalized moment-bending angle curves (**Fig. 2c**) and all hexagonal rings are still foldable. However, a larger corner radius of the hexagonal ring leads to a slightly less stable folding and a more rounded peach core shape at the folded state, which still demonstrates approximately the same 11% of the initial area. Then, using the same foldable ring (h/t = 5, r/a = 0.3, a/t = 200), we investigate the influence of ring size (a/t = 50, 100, 200, 300, and 400). From the normalized moment-bending angle curves (**Fig. 2d**), increasing the ring size does not significantly affect the foldability and stability, nor the folded shape of the hexagonal ring. To validate the FEA simulation, a hexagonal ring (h/t = 5, r/a = 0.3, and a/t = 200) is 3D-printed to experimentally demonstrate the bending-induced snap-folding. In **Fig. 2e**, the top row illustrates

the FEA simulation of the stable snap-folding process, and the bottom row shows the experimental verification, which agrees with the FEA prediction.

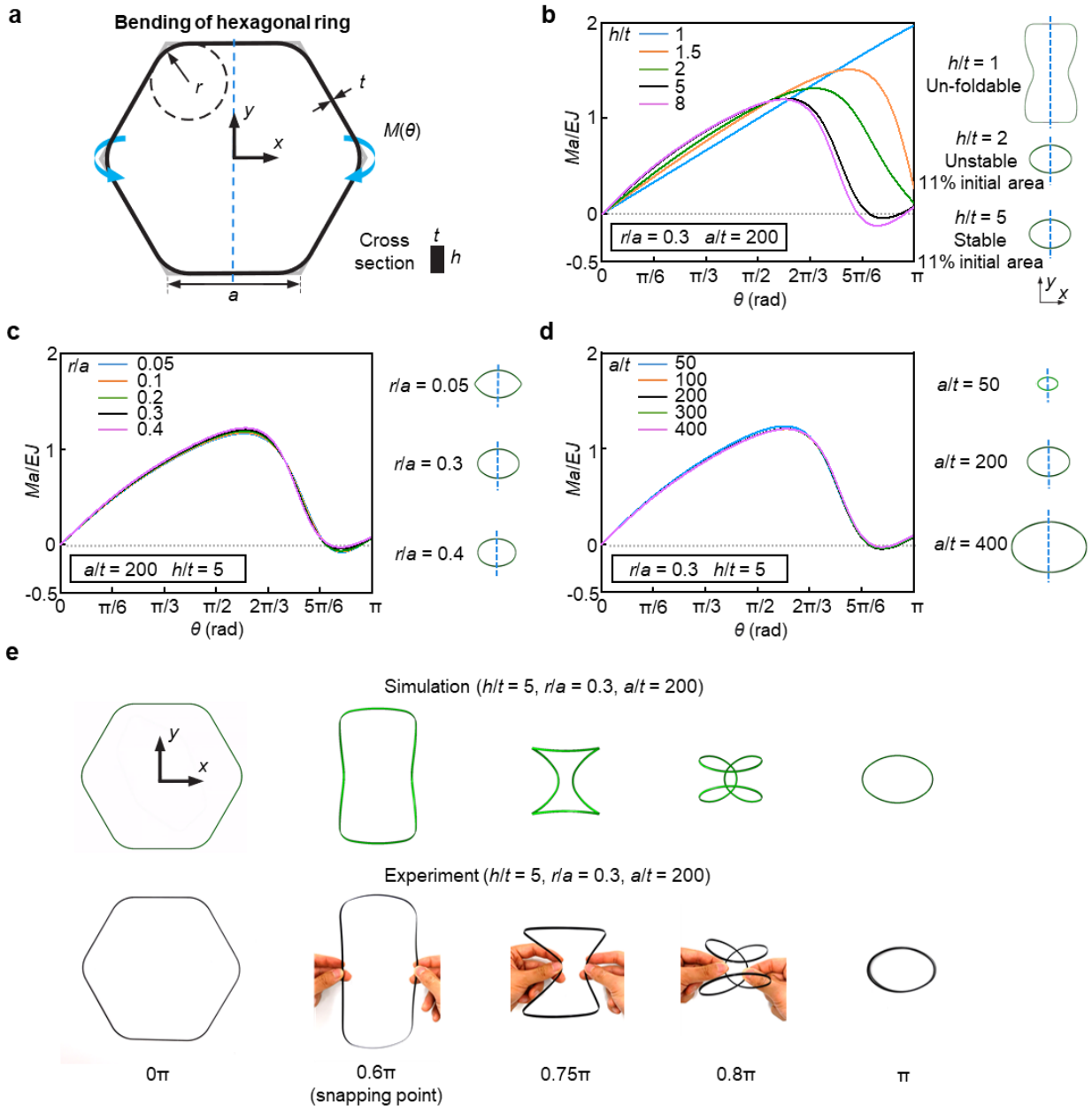

Fig. 2. FEA and experimental results of the snap-folding of hexagonal rings via bending applied at two corners that pass the centerline of the ring. (a) Geometric parameters and loading conditions of the hexagonal ring. (b-d) FEA results of normalized moment-bending angle curves for hexagonal rings with varied (b) cross-sections, (c) corner radii, and (d) ring sizes. (e) Comparison of FEA simulation and experimental verification of a hexagonal ring with stable folding.

2.2 Influence of loading locations on the bending-induced folding

In this section, we study how the loading locations of bending influence the folding behavior of hexagonal rings. When the loading positions pass the centerline of the hexagonal ring, bending applied at two rounded corners of the hexagonal ring is defined as “corner bend”, while bending applied at the middle of edge is defined as “edge bend” (**Fig. 3a**). The folding processes of both loading methods are characterized by normalized moment versus bending angle θ about the y-axis (dashed blue lines in **Fig. 3a**). Here, hexagonal rings are studied with a fixed hexagonal profile (r/a = 0.3, a/t = 200) and varied cross-sections (h/t = 1, 2, 5, and 8). Different loading methods, either corner bend (solid lines) or edge bend (dashed lines), do not alter the trend of normalized moment-bending angle curves (**Fig. 3b**). The foldability and stability of the hexagonal ring are mainly determined by the ring’s cross-section aspect ratio h/t. The hexagonal rings are un-foldable for h/t = 1, foldable but unstable for h/t = 2, and foldable and stable for h/t = 5, 8. For foldable rings, the curve of edge bend method shows a slightly higher normalized moment than that of corner bend method, while having a comparable bending angle at the snapping point. **Fig. 3c** demonstrates detailed snap-folding processes of a hexagonal ring (h/t = 5, r/a = 0.3, a/t = 200) via corner bend and edge bend methods, illustrating the folding flexibility of the hexagonal ring for a stable snap-folding.

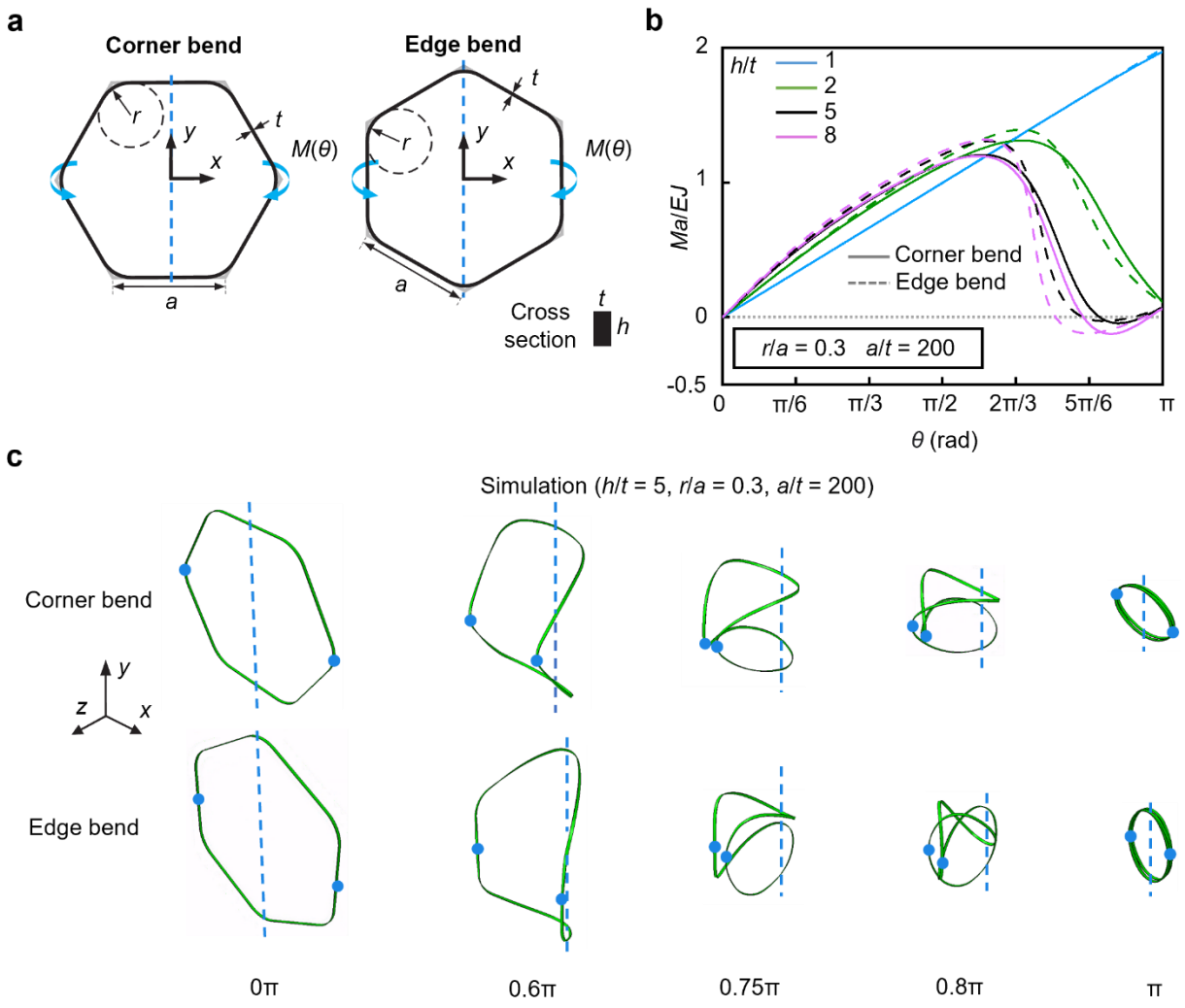

Fig. 3. FEA simulations of two types of bending-induced snap-folding with loading locations passing the centerline of the hexagonal ring. (a) Bending applied at either the corner or the middle of edge. (b) Normalized moment versus bending angle of hexagonal ring folding with varied cross-sections. (c) Folding processes of a hexagonal ring by bending applied at either the corner or the middle of edge. The blue dots denote the locations where bending is applied.

We next study bending-induced snap-folding with loading locations offset along the edge. Based on the corner bend method, the loading positions of bending can offset from corners along the edge of the hexagonal ring while having the same bending axis (the *y*-axis in **Fig. 4a**). The bending angle θ is defined as the amount of rotation applied at the loading locations about the *y*-axis. The orange, green, and pink dots are loading locations with an offset of $a/4$, $a/2$, and $3a/4$

from the corners (blue dots), respectively. **Fig. 4b** illustrates the corresponding normalized moment-bending angle curves with different loading locations of a hexagonal ring (h/t = 5, r/a = 0.3, a/t = 200). The hexagonal ring is always foldable and stable via bending at four locations, and a larger offset requires a slightly higher moment to trigger snapping. For the deformation of the ring during folding, applying loadings off the hexagon centerline breaks the symmetry of ring about the *xz*-plane, as shown by the configurations at snapping in **Fig. 4c**. However, the folded configuration of hexagonal ring is independent of bending locations, illustrating the self-guided deformation and stable folded configuration insensitive to external perturbation. Note that the bending angle has different values at the folded state because it is separately defined at different loading locations.

Similarly, the bending locations of the edge bend method can offset along the edge from its middle position, while keeping the same bending axis (the *y*-axis in **Fig. 5a**). The bending angle θ is the amount of rotation at the loading locations about the *y*-axis. The orange and pink dots are loading locations with an offset of $a/4$ and $a/2$ along the edge from the middle (blue dots), respectively. **Fig. 5b** shows normalized moment-bending angle curves during folding of a hexagonal ring (h/t = 5, r/a = 0.3, a/t = 200) at different locations. Still, the foldability and stability of the hexagonal ring are not affected by the loading locations, and a larger offset requires a higher moment at the snapping point. As shown in **Fig. 5c**, while different intermediate configurations are observed when bending location differs, the folded configuration of the hexagonal ring is the same, with 11% of its initial area. In summary, the hexagonal rings can be folded precisely in a self-guided manner with a high tolerance to the variations in the loading conditions.

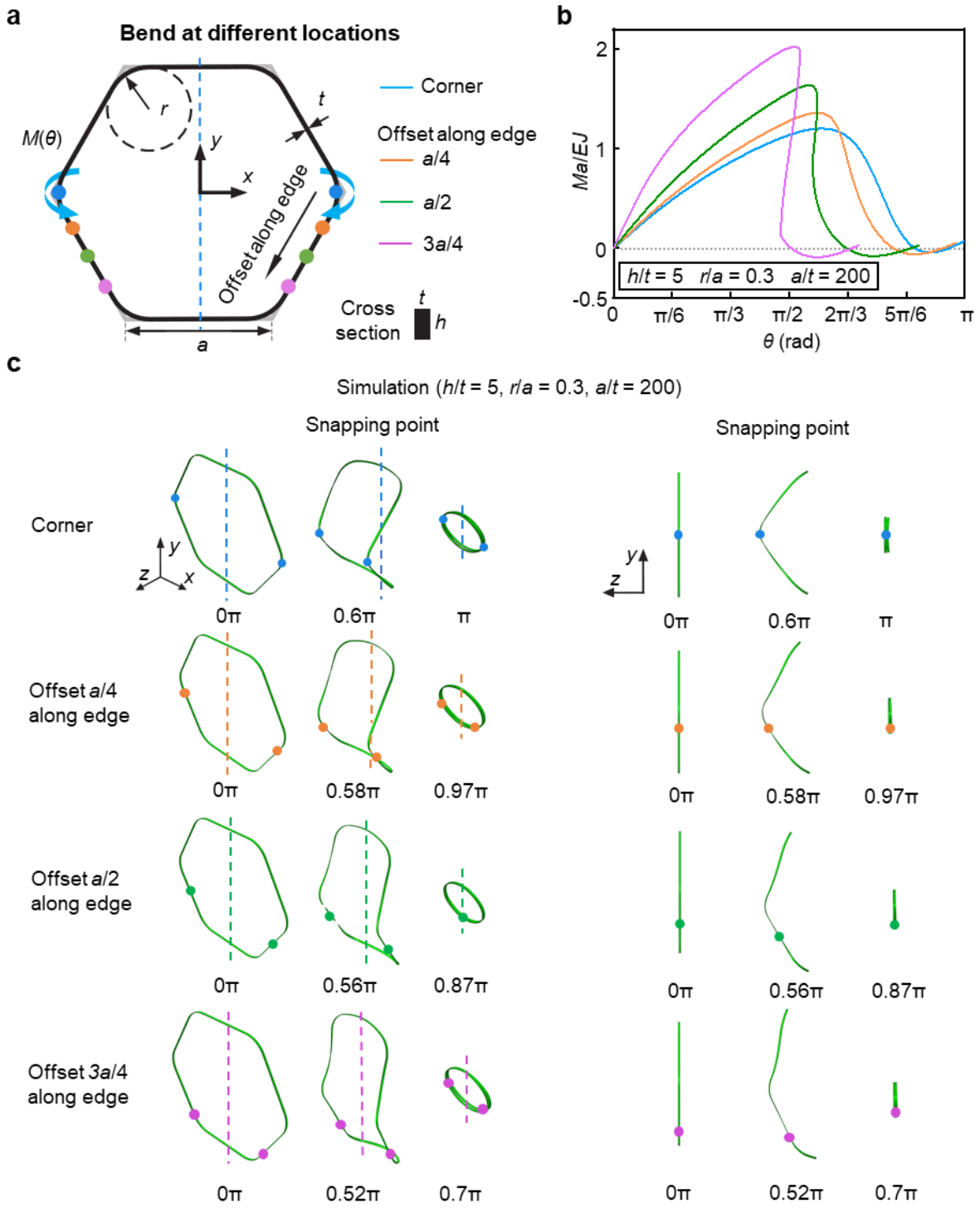

Fig. 4. FEA simulations of bending-induced folding with loading locations offset from corners of the hexagonal ring along the edge. (a) Loading locations with different offsets along the edge. (b) Normalized moment versus bending angle with varying offsets along the edge. (c) Isometric view and side view of the hexagonal ring at the initial, snapping, and folded configurations with different loading locations.

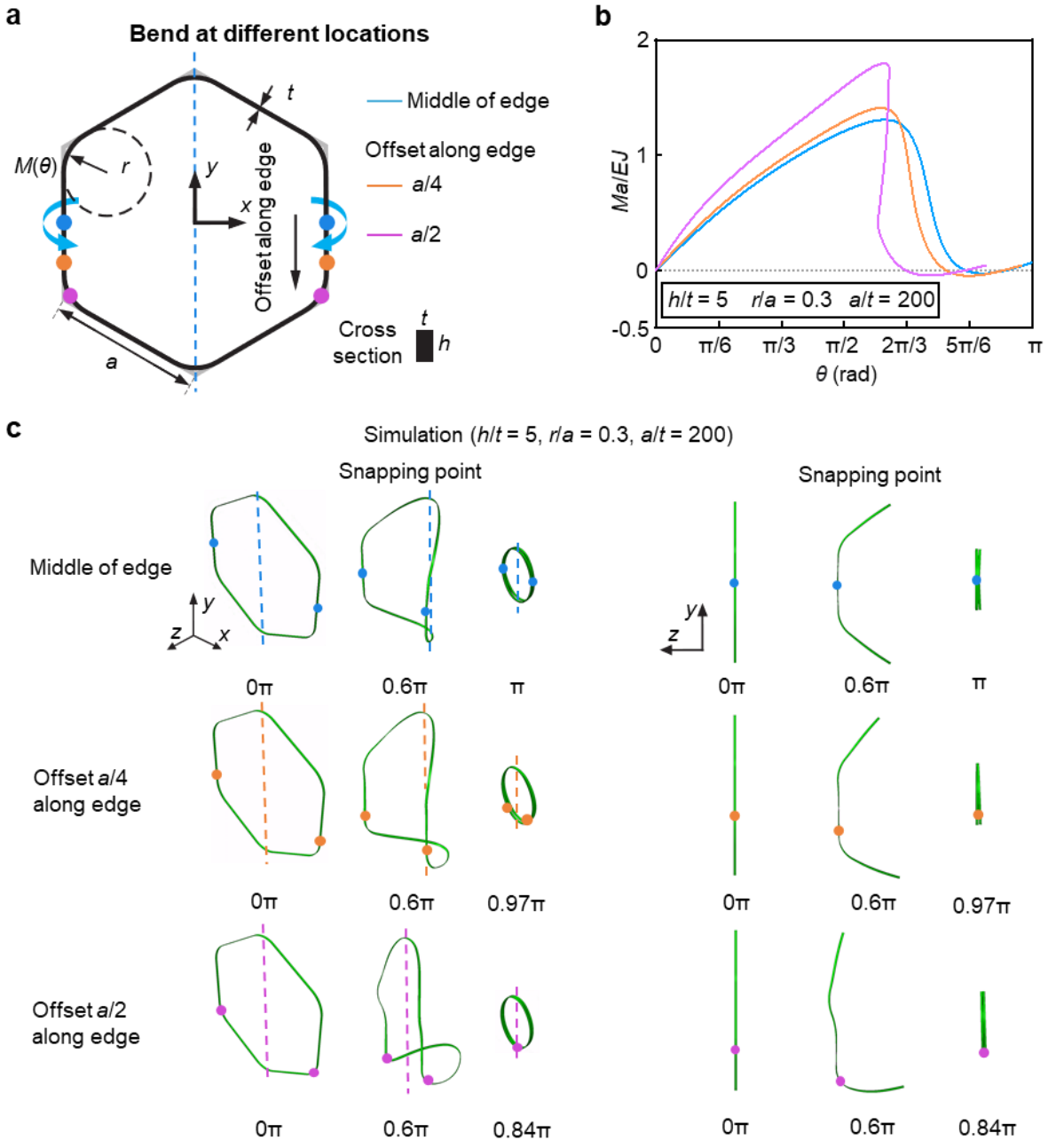

Fig. 5. FEA simulations of bending-induced folding with loading locations offset from the middle along the edge. (a) Loading locations with different offsets along the edge. (b) Normalized moment versus bending angle with varying offsets from the middle along the edge. (c) Isometric view and side view of the hexagonal ring at the initial, snapping, and folded configurations with different loading locations.

3 Twisting-induced Snap-Folding of Hexagonal Rings

3.1 Influence of hexagonal ring geometry on twisting-induced folding

An alternative loading method, twisting, can also induce snap-folding of hexagonal rings. In this section, we study the influence of ring geometry, namely cross-section aspect ratio, edge length, and corner radius, on the twisting-induced folding of hexagonal rings. In FEA, twisting motion is enforced by a pair of rotations about the x-axis (dashed orange line) on two corners of the hexagonal ring in reverse directions (**Fig. 6a**). Here, the twisting angle δ from 0 to π is applied at two corners that pass the centerline of the hexagon. The two loading positions are free to slide inward along the x-axis direction Twisting at different locations is studied as well in the next section. **Fig. 6b** shows the normalized moment-twisting angle curves of hexagonal rings (r/a = 0.3, a/t = 200) with varied cross-section aspect ratios (h/t = 1, 1.5, 2, 5, and 8). When h/t = 1 or 1.5 (blue and orange curves), the moment increases first and then decreases slightly before climbing up again, indicating an un-foldable behavior under twisting. For a foldable ring, the normalized moment first gradually increases with the twisting angle. It then shows a steep drop after the snapping point, and slowly decreases toward zero moment while the ring folds into the configuration of three overlapping rings. With a higher h/t value, the hexagonal ring is foldable but unstable (h/t = 2, green curve) and foldable and stable (h/t = 5, black curve) via twisting. Compared to the bending-induced folding, the hexagonal ring with h/t = 8 is un-foldable via pure twisting (pink solid line in **Fig. 6b**). See Fig. S2 for detailed twisting-induced folding processes with varied cross-section aspect ratios. However, adding only a small bending component during the twisting motion can trigger stable snap-folding for the hexagonal ring with h/t = 8 (dashed pink line). Here, the bending component is induced by adding a pair of modest pushing forces on the corners where twisting is applied (see Fig. S3 for the influence of applied forces on snap-folding process). The small bending perturbation does not greatly alter the normalized moment-twisting

angle curve or the deformation configurations before the snapping point while setting off the snapping.

Then, using a foldable ring (h/t = 5, r/a = 0.3, a/t = 200), we investigate the influence of corner radius (r/a =0.05, 0.1, 0.2, 0.3, and 0.4) on the twisting-induced folding process. The hexagonal rings with a relatively small radius (r/a =0.05, 0.1, 0.2) are un-foldable via twisting only, as shown by the overall increasing normalized moment in **Fig. 6c**. However, these un-foldable rings under pure twisting can achieve snap-folding when a small bending component is added, for example, the hexagonal ring with r/a =0.05 (dashed blue curve in **Fig. 6c**, see Fig. S4 for the influence of applied forces on snap-folding process). By increasing the corner radius (r/a =0.3, 0.4), hexagonal rings show an easier twisting-induced snap-folding with a slightly less stable folded state. It should be noted that, as long as the ring is folded, the peach core-shaped configuration (~11% of the initial area) and the stability of folded ring are solely determined by the ring geometry. Influence of hexagonal ring size on twisting-induced folding is also investigated (a/t = 50, 100, 200, 300, and 400) based on the same foldable ring (h/t = 5, r/a = 0.3, a/t = 200). For hexagonal rings with a/t ranging from 100 to 400, increasing the ring size does not significantly affect the foldability of the hexagonal ring via twisting (**Fig. 6d**). The foldable rings demonstrate similar stable folded configurations. Although a smaller hexagonal ring (a/t = 50) is not foldable by twisting only, employing an extra bending component with twisting is enough to induce stable snap-folding (see Fig. S5 for the influence of applied forces on snap-folding process). A hexagonal ring with geometry of h/t = 5, r/a = 0.3, and a/t = 200 is 3D-printed to validate twisting-induced folding simulation. In **Fig. 6e**, the FEA prediction (Top row) agrees well with the experimental verification (Bottom row), showing a stable folding process via twisting motion.

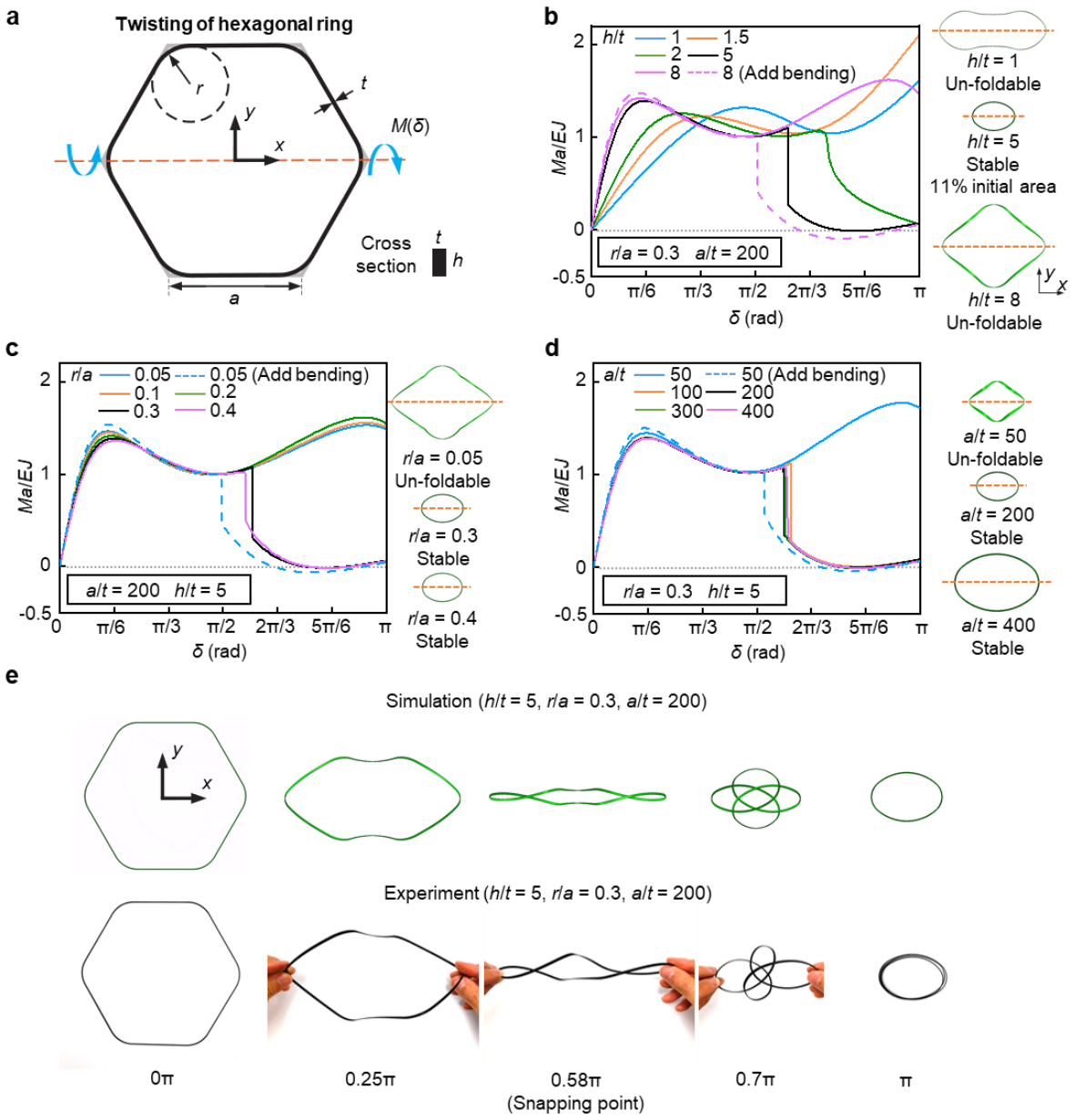

Fig. 6. FEA and experimental results of the snap-folding of hexagonal rings via twisting applied at two corners that pass the centerline of the ring. (a) Geometric parameters and loading conditions of the hexagonal ring. (b-d) FEA results of normalized moment-twisting angle curves for hexagonal rings with varied (b) cross-sections, (c) corner radii, and (d) ring sizes. (e) Comparison of FEA simulation and experimental verification of a hexagonal ring with stable folding.

3.2 Influence of loading locations on the twisting-induced folding

In this section, we study the influence of twisting locations on the twisting-induced folding behavior of hexagonal rings. When the loading positions pass the centerline of the hexagonal ring, twisting applied at two rounded corners of the hexagonal ring is defined as “corner twist”, while twisting applied at the middle of edge is defined as “edge twist” (**Fig. 7a**). The folding processes of both corner twist and edge twist methods are characterized by the normalized moment-twisting angle δ about the x-axis (dashed orange lines in **Fig. 7a**). Snap-folding via two twisting methods is studied for hexagonal rings with a fixed hexagonal profile (r/a = 0.3, a/t = 200) and varied cross-section aspect ratios (h/t = 1, 2, 5, and 8). In **Fig. 7b**, the hexagonal ring is un-foldable for h/t = 1 via both corner twist (solid lines) and edge twist (dashed lines) methods, showing approximately the same normalized moment-twisting angle curves. For hexagonal rings with h/t = 2 or 5, the twisting locations do not change the ring’s foldability and stability (foldable but unstable for h/t = 2, and foldable and stable for h/t = 5). The corner twist method exhibits a slightly higher normalized moment before the snapping point but has about the same twisting angle. With a higher h/t of 8, the hexagonal ring is un-foldable by twisting at corners but foldable and stable by twisting at the middle of edge. Similarly, by adding a small bending component, twisting at corners can also trigger a stable folding of the hexagonal ring with h/t = 8. **Fig. 7c** demonstrates the detailed snap-folding processes of a hexagonal ring (h/t = 5, r/a = 0.3, a/t = 200) via corner twist and edge twist methods, and both loading methods show stable snap-folding with the same folded configuration.

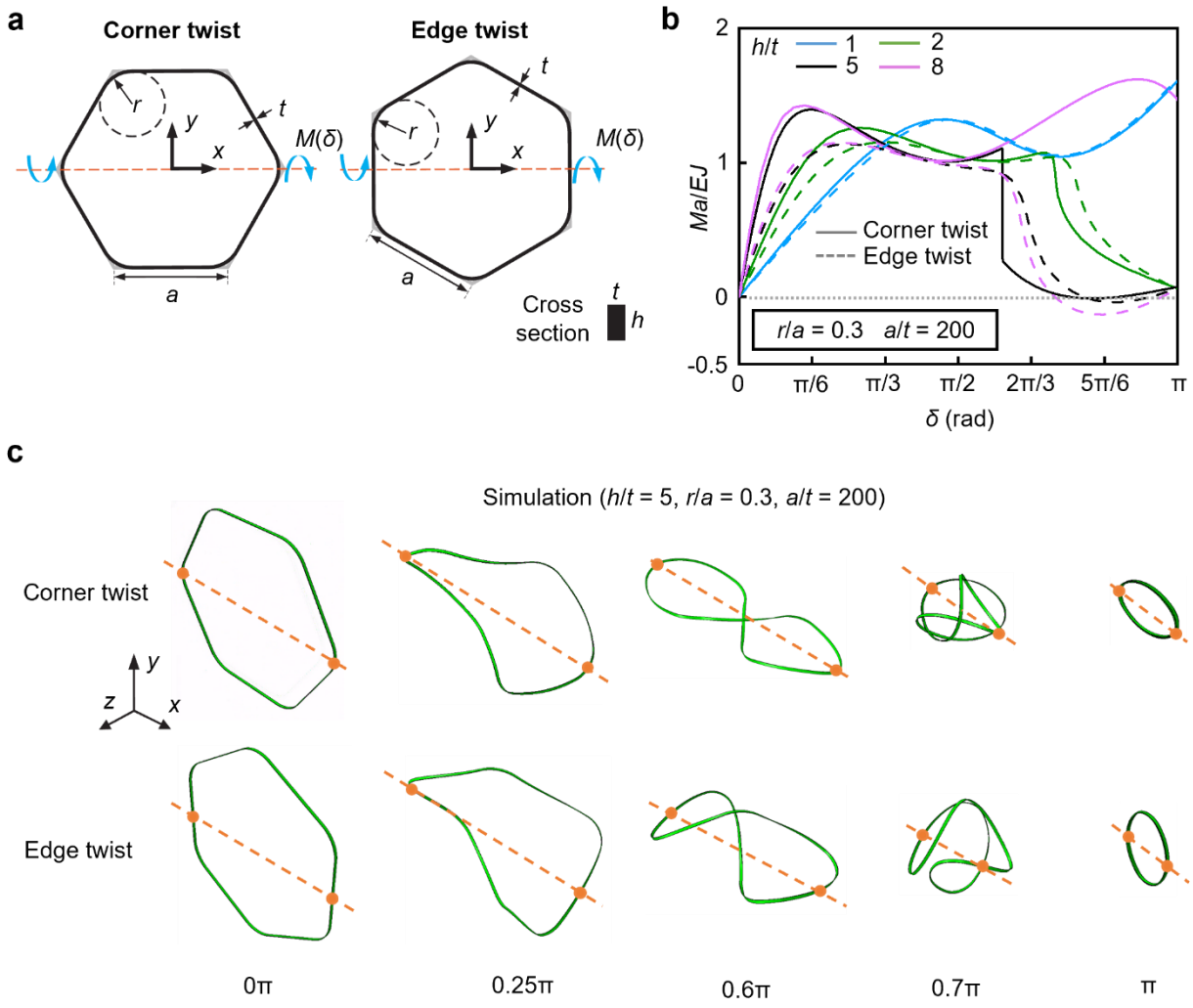

Fig. 7. FEA simulations of two types of twisting-induced snap-folding with loading locations passing the centerline of the hexagonal ring. (a) Twisting applied at either the corner or the middle of edge. (b) Normalized moment versus twisting angle of hexagonal ring folding with varied cross-sections. (c) Folding processes of a hexagonal ring by twisting applied at either the corner or the middle of edge. The orange dots denote the locations where twisting is applied.

4 Conclusions

In this work, we study the foldability and stability of the hexagonal ring's snap-folding triggered by bending or twisting. Based on the FEA simulations, a larger hexagonal ring cross-section aspect ratio plays a dominant role in increasing rings' foldability and stability. The foldable

hexagonal rings' folded state has a large packing ratio of approximately 11% of the initial hexagon area. For tessellated 2D or 3D foldable structures, the packing capability can be further enhanced by stacking and then folding hexagonal rings. Moreover, hexagonal ring origami demonstrates precise and self-guided folding with have a high tolerance to variations in loading conditions. We anticipate the high tolerance for varied loading permits applications of hexagonal ring origami with reliable folding and deploying while possessing an excellent packing capability.

Acknowledgments

R.R.Z., S.W., J.D., S.L. acknowledge National Science Foundation Award EFMA-2029643 and National Science Foundation Career Award CMMI-1943070.

Appendix A. Finite element analysis details

Snap-folding simulations of hexagonal rings are carried out using the commercial software ABAQUS 2019 (Dassault Systèmes, France). The linear brick element with reduced integration (C3D8R) is used with linear elastic material with a Young's modulus of 2 GPa and a Poisson's ratio of 0.3. We assign 6 elements through the thickness, 10 elements through the height, and ~400 elements along each edge of the hexagonal rings. A relatively small damping factor of 10^{-10} is adopted to stabilize the simulation. The boundary conditions are applied on reference points constrained with nodes of the cross-section at loading locations using multipoint constraints (MPCs). The reaction moments are exported to get normalized moment-bending angle curves and normalized moment-twisting angle curves. Since the purpose of this work is to analyze the influence of ring geometry, loading location, and loading method on the hexagonal rings' folding, self-contact during the folding process is not considered. The maximum principal strain contours

of hexagonal rings (h/t = 5, r/a = 0.3, a/t = 200 and 400) during bending-induced folding, twisting-induced folding as well as at the folded state are provided in Fig. S6-S7. During the folding process, corner twist method introduces a slightly higher strain than corner bend method does. Whereas the strain of a specific ring is the same and uniformly distributed across the ring at the folded state, independent of the folding methods. The strain is determined by the curvature of the folded ring, which is directly related to the size of the ring. The larger ring with a/t = 400 shows a lower strain (0.233%) than the ring with a/t = 200 (0.472%) at the folded state.

Appendix B. Ring fabrication

A commercial 3D printer Ultimaker S5 (Ultimaker, Netherland), is used to print hexagonal rings with polylactic acid (PLA, E = 2 GPa). A steel hexagonal ring (E = 200 GPa) is also fabricated, manually reshaped from a circular ring to demonstrate a rapid snap-folding process (Video S1).

References

1. Karihaloo, B.L., K. Zhang, and J. Wang, *Honeybee combs: how the circular cells transform into rounded hexagons.* Journal of the Royal Society Interface, 2013. **10**(86): p. 20130299.
2. Mead, F.W., *Wheel Bug, Arilus cristatus (Linnaeus)(Insecta: Hemiptera: Reduviidae): EENY086/IN243, rev. 3/2017.* EDIS, 2017. **2017**(2): p. 5-5.
3. Nilsson, D.-E., *Optics and evolution of the compound eye*, in *Facets of vision*. 1989, Springer. p. 30-73.
4. Gardner, J.P., et al., *The james webb space telescope.* Space Science Reviews, 2006. **123**(4): p. 485-606.
5. Lin, J., et al., *Design and fabrication of a three-dimensional artificial compound eye using two-photon polymerization.* Micromachines, 2018. **9**(7): p. 336.
6. Cheng, Y., et al., *Review of state-of-the-art artificial compound eye imaging systems.* Bioinspiration & biomimetics, 2019. **14**(3): p. 031002.
7. Zhang, Q., et al., *Bioinspired engineering of honeycomb structure–Using nature to inspire human innovation.* Progress in Materials Science, 2015. **74**: p. 332-400.
8. Chen, Y., Z. Jia, and L. Wang, *Hierarchical honeycomb lattice metamaterials with improved thermal resistance and mechanical properties.* Composite Structures, 2016. **152**: p. 395-402.
9. Montgomery, S.M., et al., *Recent advances in additive manufacturing of active mechanical metamaterials.* Current Opinion in Solid State and Materials Science, 2020. **24**(5): p. 100869.
10. Qi, J., et al., *Recent Progress in Active Mechanical Metamaterials and Construction Principles.* Advanced Science, 2021: p. 2102662.

11. Wu, S., et al., *Symmetry-breaking Actuation Mechanism for Soft Robotics and Active Metamaterials.* ACS Applied Materials & Interfaces, 2019. **11**(44): p. 41649-41658.
12. Kim, D.-H., et al., *Flexible and stretchable electronics for biointegrated devices.* Annual review of biomedical engineering, 2012. **14**: p. 113-128.
13. Amjadi, M., et al., *Stretchable, skin-mountable, and wearable strain sensors and their potential applications: a review.* Advanced Functional Materials, 2016. **26**(11): p. 1678-1698.
14. Hines, L., et al., *Soft actuators for small-scale robotics.* Advanced materials, 2017. **29**(13): p. 1603483.
15. Sitti, M., *Miniature soft robots—road to the clinic.* Nature Reviews Materials, 2018. **3**(6): p. 74.
16. Wu, S., et al., *Stretchable origami robotic arm with omnidirectional bending and twisting.* Proceedings of the National Academy of Sciences, 2021. **118**(36).
17. Kuribayashi, K., et al., *Self-deployable origami stent grafts as a biomedical application of Ni-rich TiNi shape memory alloy foil.* Materials Science and Engineering: A, 2006. **419**(1-2): p. 131-137.
18. Chen, T., et al., *Autonomous deployment of a solar panel using elastic origami and distributed shape-memory-polymer actuators.* Physical Review Applied, 2019. **11**(6): p. 064069.
19. Zirbel, S.A., et al., *Accommodating thickness in origami-based deployable arrays.* Journal of Mechanical Design, 2013. **135**(11).
20. Callens, S.J. and A.A. Zadpoor, *From flat sheets to curved geometries: Origami and kirigami approaches.* Materials Today, 2018. **21**(3): p. 241-264.
21. Filipov, E.T., T. Tachi, and G.H. Paulino, *Origami tubes assembled into stiff, yet reconfigurable structures and metamaterials.* Proceedings of the National Academy of Sciences, 2015. **112**(40): p. 12321-12326.
22. Kotikian, A., et al., *3D printing of liquid crystal elastomeric actuators with spatially programed nematic order.* Advanced Materials, 2018. **30**(10): p. 1706164.
23. Novelino, L.S., et al., *Untethered control of functional origami microrobots with distributed actuation.* Proceedings of the National Academy of Sciences, 2020. **117**(39): p. 24096-24101.
24. Roach, D.J., et al., *Novel ink for ambient condition printing of liquid crystal elastomers for 4D printing.* Smart Materials and Structures, 2018. **27**(12): p. 125011.
25. Jin, B., et al., *Programming a crystalline shape memory polymer network with thermo-and photo-reversible bonds toward a single-component soft robot.* Science advances, 2018. **4**(1): p. eaao3865.
26. Kuang, X., et al., *Magnetic Dynamic Polymers for Modular Assembling and Reconfigurable Morphing Architectures.* Advanced Materials, 2021: p. 2102113.
27. Yu, L., et al., *Rapid fabrication of malleable fiber reinforced composites with vitrimer powder.* ACS Applied Polymer Materials, 2019. **1**(9): p. 2535-2542.
28. Zhao, R. and X. Zhao, *Multimodal surface instabilities in curved film–substrate structures.* Journal of Applied Mechanics, 2017. **84**(8).
29. Shan, S., et al., *Multistable architected materials for trapping elastic strain energy.* Advanced Materials, 2015. **27**(29): p. 4296-4301.
30. Haghpanah, B., et al., *Multistable shape-reconfigurable architected materials.* Advanced Materials, 2016. **28**(36): p. 7915-7920.
31. Liu, F., et al., *Machine learning-based design and optimization of curved beams for multistable structures and metamaterials.* Extreme Mechanics Letters, 2020. **41**: p. 101002.
32. Li, B., et al., *Mechanics of morphological instabilities and surface wrinkling in soft materials: a review.* Soft Matter, 2012. **8**(21): p. 5728-5745.
33. Wu, S., et al., *Ring Origami: Snap-Folding of Rings with Different Geometries.* Advanced Intelligent Systems, 2021. **3**(9): p. 2100107.
34. Yan, Z., et al., *Controlled mechanical buckling for origami-inspired construction of 3D microstructures in advanced materials.* Advanced functional materials, 2016. **26**(16): p. 2629-2639.

35. Wu, G., et al., *Directing the deformation paths of soft metamaterials with prescribed asymmetric units.* Advanced Materials, 2015. **27**(17): p. 2747-2752.
36. Gao, W., et al. *Hexamorph: A reconfigurable and foldable hexapod robot inspired by origami*. in *2014 IEEE/RSJ International Conference on Intelligent Robots and Systems*. 2014. IEEE.
37. Overvelde, J.T., et al., *Rational design of reconfigurable prismatic architected materials.* Nature, 2017. **541**(7637): p. 347-352.
38. Li, S., et al., *Liquid-induced topological transformations of cellular microstructures.* Nature, 2021. **592**(7854): p. 386-391.
39. Zhang, Y.-J., et al., *Hexagon-twist frequency reconfigurable antennas via multi-material printed thermo-responsive origami structures.* Frontiers in Materials, 2020. **7**: p. 417.
40. Zhao, Z., et al., *Stiff reconfigurable polygons for smart connecters and deployable structures.* International Journal of Mechanical Sciences, 2019. **161**: p. 105052.